Additive manufacturability of superalloys: Process-induced porosity, cooling rate and metal vapour

Chinnapat Panwisawas, Yilun Gong, Yuanbo Tony Tang, Roger C. Reed, Junji Shinjo

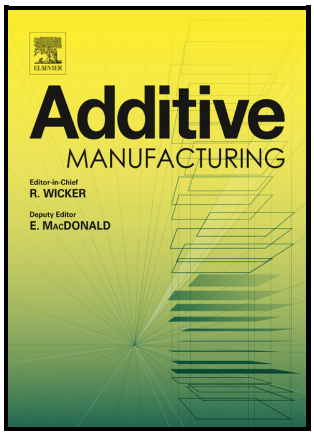

PII: S2214-8604(21)00497-8

DOI: https://doi.org/10.1016/j.addma.2021.102339

Reference: ADDMA102339

To appear in: *Additive Manufacturing*

Received date: 16 June 2021
Revised date: 3 September 2021
Accepted date: 15 September 2021

Please cite this article as: Chinnapat Panwisawas, Yilun Gong, Yuanbo Tony Tang, Roger C. Reed and Junji Shinjo, Additive manufacturability of superalloys: Process-induced porosity, cooling rate and metal vapour, *Additive Manufacturing,* (2021) doi:https://doi.org/10.1016/j.addma.2021.102339

Additive manufacturability of superalloys: Process-induced porosity, cooling rate and metal vapour

Chinnapat Panwisawas[1,2,*], Yilun Gong[2], Yuanbo Tony Tang[2], Roger C. Reed[2,3], Junji Shinjo[4]

[1]School of Engineering, University of Leicester, University Road, Leicester LE1 7RH, United Kingdom

[2]Department of Materials, University of Oxford, Parks Road, Oxford OX1 3PH, United Kingdom

[3]Department of Engineering Science, University of Oxford, Parks Road, Oxford, OX1 3PJ, United Kingdom

[4]Next Generation Tatara Co-Creation Centre (NEXTA), Shimane University, 1060, Nishikawatsu, Matsue 690-8504, Japan

*corresponding author: chinnapat.panwisawas@leicester.ac.uk

Abstract

Digital technology such as metal additive manufacturing (AM) provides flexible process design freedom to fabricate intricate three-dimensional structures layer-by-layer. However, its manufacturability relies on the fundamental understanding of melt pool physics and fluid (metal) dynamics. The effect of metal vapour and porosity induced during the laser-materials interaction can influence the additive manufacturability. In this work, composition-process relationship of laser-based powder-bed fusion (L-PBF) AM is studied via computational fluid dynamics modelling to rationalise solid-liquid-vapour transformation where empirical-based approach is used to generate thermo-physical property of about 100 nickel-based superalloys at the liquid state. It is found that with larger vapor mass loss, the porosity tends to be higher. However, the higher vapour mass loss means faster cooling rate. This is indicated that the thermal-fluid flow process, which is also governed by the thermo-physical property, strongly affects the additive manufacturability. Additive manufacturability map based upon porosity, cooling rate from liquid to solid, volatile mass loss criteria has been established to link the composition in nickel-based superalloys with their thermo-physical property. This offers a thermal-fluid science based tool in designing compositions of novel superalloys for AM applications.

Keywords: Metal vapour, Liquid metal, Thermal-fluid dynamics, Additive Manufacturability, Superalloys

Introduction

Metal additive manufacturing (AM) or 3D printing is one of the digital technologies in the fourth industrial revolution – so called the 'Industry 4.0' [1-3]. Ranging from biomedical stent in artery to aerojet turbine blades, consecutively adding materials layer-by-layer enables sophisticated parts to be printed. It prevails over the conventional subtractive approaches, *e.g.* casting, machining, and cutting, in that the AM allows complicated 3D shapes to be created timely and cost effectively [4-8]. Aerospace engine parts for combustors and turbines need to be highly heat-resistant in order to realise high engine efficiency, and currently Ni-based superalloys are best suited. At the same time, complicated flow passage shapes should be manufactured accurately with fewer manufacturing processes, which makes AM a promising candidate [3]. Nevertheless,

printing a metal especially for aerospace usage requires fundamental understanding in physical phenomena such as melting, evaporation [9-14] and even ionisation to form plasma [15]. Literature has focused on researching at temperatures close to the solid state rather than the liquid state conditions, for not only technological importance but scientific reasons [16-19]. Besides, the solid-liquid transition based upon computational thermodynamics typically assumed equilibrium conditions (or local-equilibrium conditions at phase interfaces), *e.g.* in conventional casting situation, and subsequently physical metallurgy and solid mechanics are applied to rationalise the material behaviour. This might not be the case for AM where the temperature can go above boiling point. At such extreme conditions, the solid-liquid-vapour transition becomes crucial, particularly, relevant fluid mechanics should be re-visited, and the significant role played by the metal vapour [4,6,20] needs to be rationalised. Non-equilibrium database for thermo-physical properties used to simulate the AM, especially for the liquid state, is required for establishing processing-structure-property-performance relationship theoretically, experimentally and computationally for materials design and innovative processes.

The need for AM requires to consider the melt flow behaviour, apart from the solid state cracking, to assess additive manufacturability or 3D printability in order to minimise thermal residual and to ensure that upon rapid cooling to ambient temperature the AM part is safe to defects in the finish pieces [17, 19]. Particularly, the flow behaviour of liquid (which is described by the Reynold number, Re) and the transport phenomena in liquid (which is characterised by the Péclet number, Pe) need to be studied. This is of significant importance to AM in nickel-based superalloys for aerospace and land-based power generation applications, where the structural integrity is often compromised by cracks and pores [19, 21-22]. In this work, we define good additive manufacturability as (i) the one of less propensity to suffer from porosity, due to both gas related porosity and lack of fusion, (ii) slower cooling rate from liquid to solid to retard residual stress and cracking, and (iii) less volatile mass loss during the L-PBF AM process. These additive manufacturability criteria are to be useful for additive manufacturing of nickel-based superalloys. The criterion (i) is related to the defect formation and the criterion (iii) is related to the local composition change, which are all directly linked with the mechanical properties of the final product (ii). It is challenging to steer the maximum synergy between experiments and modelling to determine a materials and processing design rule for AM which is physically sound [23-25].

Nickel-based superalloy is a high temperature material which is strengthened by γ' intermetallics embedded in a highly concentrated Ni solid-solution matrix, γ. Typically, γ' strengthening through optimising the Al and Ti contents (Ni_3(Al, Ti), with the structure $L1_2$) to obtain desired γ' volume fraction to ensure the high temperature performance such as creep and fatigue [26-29]. Therefore, temperature regime that is important to produce or design the superalloys is traditionally around the melting point. However, with the variabilities of AM process, metal vapour can be possible even when manufacturing the considered-to-be printable alloys, such as IN718, IN625 [16] which also suffer from porosity and mass loss. It is thus now significant to review

some rudimentary of chemical species for superalloys and relate it to the liquid flow property for assessing and rationalising the physical effects which govern the microstructure variation and site specific property induced from the AM process [17]. It is also of significance that the chemistry-process relationship should be studied in AM of nickel-based superalloys to establish the criteria of additive manufacturability, see Figure 1, where the porosity is caused by the vapourised gas phase in the liquid. The melt pool dynamics has been intensively investigated due to its importance in determining the porosity characteristics and the final product quality [9,30-33], but the systematic parametric study has not been well done so far, only with some pioneering work [10].

Therefore, the first objective of this study is to systematically assess the liquid-flow physical properties for over 100 Ni-based superalloys depending on the chemical composition, which will give insights into selecting suitable superalloy properties for L-PBF AM applications. The second objective is to investigate the melt pool dynamics in terms of porosity formation, resulting cooling rate and mass loss quantitatively over the variation range of physical properties suggested by the above first part. The process parameters of Re and Pe will be also discussed. This will more thoroughly help the understanding of the additive manufacturability in addition to the knowledge of the previous work [10].

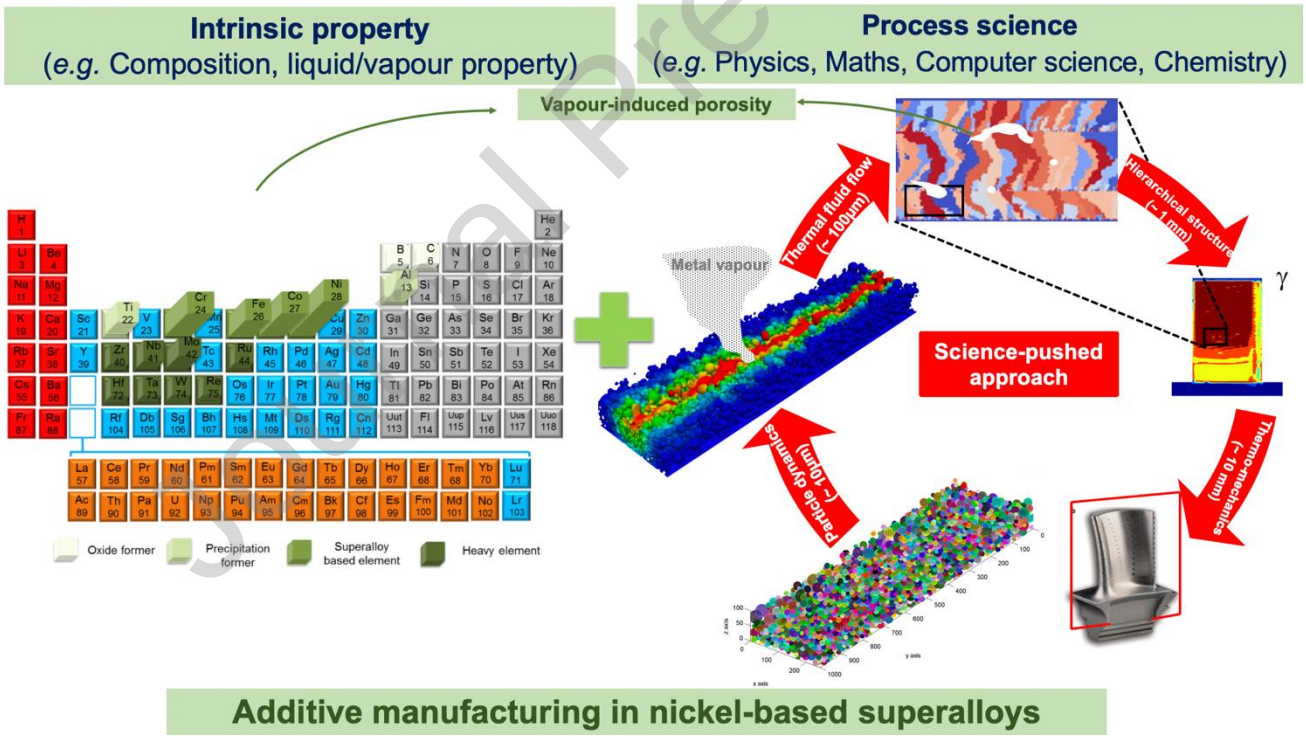

Figure 1: Schematic illustration of linking the intrinsic property with the multi-scale process science, emphasising the role of metal vapour to porosity, after [34].

Method

Thermal-chemical-physical property

Successful adoption of metal AM is to understand the underlying mechanisms of process-induced microstructure, emerging property and defect formation in order to optimise the 3D fabricated performance. One of the key defects in AM is porosity, either melt flow induced or lack-of-fusion types, and this is caused by the capture of vapourised gas phases in the liquid [5, 35]. Vapourisation (liquid to vapour phase transition) takes place when the temperature is above the boiling point (at certain pressures) of the materials – both on the surface (so-called evaporation) and in the bulk – and it alters the state of the materials to be metal vapour in superalloy case [35-37]. This might happen when the high energy heat source results in keyhole fusion mode rather than conduction melting one [16]. Computational framework for composition-process-structure-property, Figure 2(a), is required to warrant the additive manufacturability [38]. It is important to emphasise that thermo-physical properties of main metallic systems, especially liquid properties, are compositional-dependent; those include melting point, (pressure-dependent) boiling points, thermal conductivity, density, and viscosity, see Figure 2(b). Chemical compositions of superalloys, typically comprised of 10-25 elements, can be categorised into four groups: relatively the same atomic weight as the base metals (Ni, Co, Fe, Cr), γ' strengthening phase former elements (Al, Ti), heavy elements (W, Mo, Hf, Re, Ta, Nb, Zr), and metalloids (C or B). The contribution of minor elements can be even more significant if some elements are more favourable to vapourisation or segregation. Figure 2(c) reveals that the vapour pressure of Al, Cr and Fe is higher than that of heavy elements and those elements are prone to vaporise first, whereas the heavy elements may segregate in the melt superalloys given that the peak temperature induced by heat source is about 3000 ^{o}C. It should be emphasised that the amount of vapour might also influence the porosity which is locally captured by the liquid metal behaviour.

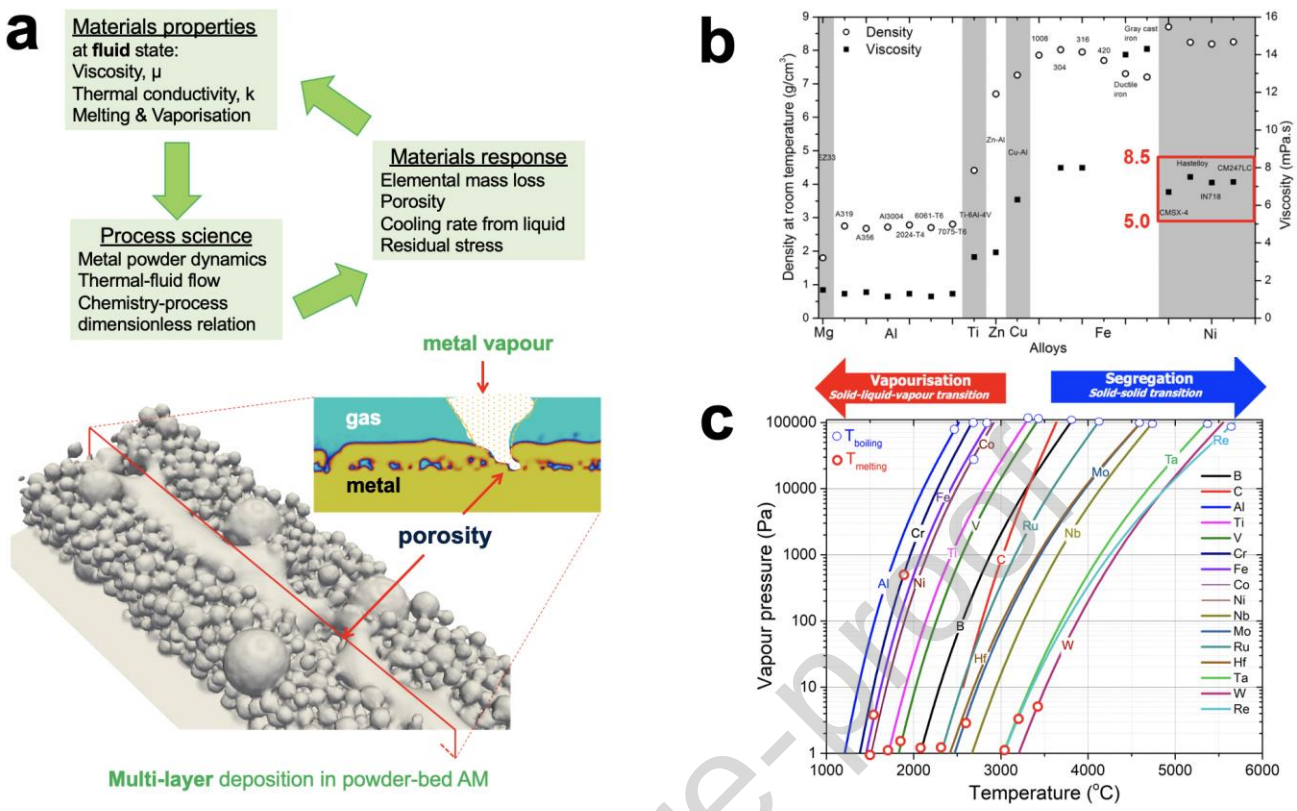

Figure 2: (a) Process-materials relationship for vapourisation; (b) measured density and dynamic viscosity for Mg, Al, Ti, Zn, Cu, Fe and Ni alloys; (c) temperature dependence of vapour pressure in the main elements of nickel-based superalloys, after [34].

Thermal-solutal-fluid flow dynamics

To further investigate the thermal fluid flow characteristics giving rise to surface structure, porosity development and microstructure simulation, a computational fluid dynamics (CFD) calculation method using our in-house CFD code called TATM-MEX has been developed to model the interaction between the laser heat source and the powder materials [39], which is illustrated in Figure 1. In the model, all interfacial phenomena present within the L-PBF AM process, including surface tension (capillary force), Marangoni's flow (thermo-capillary force) and recoil pressure have been incorporated in simulation [39]. The heat loss due to vaporisation, conduction, convection and radiation have also been taken into account in this work. The code can also treat multiple elements by solving the species mass fraction equations including diffusion. The liquid/gas interface is captured by the level-set method, combined with the volume-of-fluid method to assure volume conservation. The governing equations for continuity, momentum, energy and mass fractions are, respectively,

$$\frac{\partial \rho}{\partial t} + (\mathbf{u} \cdot \nabla)\rho = -\rho \nabla \cdot \mathbf{u}$$

$$\frac{\partial \mathbf{u}}{\partial t} + (\mathbf{u} \cdot \nabla)\mathbf{u} = -\frac{\nabla p}{\rho} + \mathbf{Q_u} + \mathbf{F}_{\mathbf{u},surf}$$

$$\frac{\partial T}{\partial t} + (\mathbf{u} \cdot \nabla)T = -\frac{p\nabla \cdot \mathbf{u}}{\rho c_p} + Q_T + \frac{1}{\rho c_p} q_L \quad (1)$$

$$\frac{\partial Y_i}{\partial t} + (\mathbf{u} \cdot \nabla)Y_i = \frac{1}{\rho} \nabla \cdot (\rho D \nabla Y_i)$$

where ρ is the density, $\mathbf{u}$ is the velocity, T is the temperature, p is the pressure, D is the diffusion coefficient and Y_i is the mass fraction of species i. The ambient gas is air and the species i include N_2, O_2 and the metal vapour element. $\mathbf{Q_u}$ represents the Newtonian viscous force, given by

$$Q_{u,i} = \frac{1}{\rho} \frac{\partial \tau_{ij}}{\partial x_j}, \quad \tau_{ij} = \mu \left(\frac{\partial u_i}{\partial x_i} + \frac{\partial u_j}{\partial x_i} \right) - \frac{2}{3} \mu \nabla \cdot \mathbf{u} \delta_{ij}. \quad (2)$$

$\mathbf{F_{u,surf}}$ represents the interfacial surface tension force including the Marangoni effect, formulated by the continuum surface force (CSF) method as,

$$\boldsymbol{F}_{\mathbf{u},surf} = \sigma \kappa \mathbf{n} |\nabla \phi| + \frac{d\sigma}{dT} (\nabla T - (\nabla T \cdot \mathbf{n})\mathbf{n}) |\nabla \phi|. \quad (3)$$

Q_T is the heat transport term, including heat conduction by Fourier's law, enthalpy transport by mass diffusion, viscous work, latent heat for phase change and radiative heat transfer,

$$Q_T = \frac{1}{\rho c_p} \left[\nabla \cdot (\lambda \nabla T) - \nabla \cdot (\rho \sum h_i Y_i V_i) + \frac{\partial \tau_{ij} u_i}{\partial x_j} - \frac{D \sum \rho Y_i \Delta h_i}{Dt} \right] + \varepsilon \sigma_{SB} (T^4 - {T_0}^4) |\nabla \phi| \quad (4)$$

where V_i is the diffusion velocity formulated by Fick's law. Δh_i is the latent heat of species i. Radiation is included on the heated metal surface identified by the gradient of the colour function $|\nabla \phi|$, with σ_{SB} the Stefan-Boltzmann constant and ε the emissivity.

The level-set function F is used to capture the shape of the liquid/gas interface. F is a signed distance function where F=0 represents the interface, F>0 the liquid phase and F<0 the gas phase. It follows

$$\frac{\partial F}{\partial t} + (\mathbf{u} \cdot \nabla)F = -|\nabla F| s_L, \quad (5)$$

where s_L is the surface regression speed due to vaporisation. To use F in determining the physical properties, it is converted into the colour function ϕ, a Heaviside function of F. For example, the density is given by $\rho = (1-\phi)\rho_G + \phi\rho_L$ where ρ_L and ρ_G are the liquid and gas density, respectively.

In this code, ray tracing is used for heat calculation. The laser beam is assumed to be composed of thousands of rays and the trajectory of each ray is traced. Reflection at the surface is assumed to be mirror reflection depending on the local surface inclination and the surface absorption factor is set at 0.6. q_L in Eq. (1) is the volumetric laser heat. The corresponding jump conditions due to phase change are given at the vaporising surface. The heat balance at the liquid/gas surface gives

$$\Delta h \dot{m}_v = \left[I - \lambda \nabla T \cdot \mathbf{n} - \sigma \varepsilon (T^4 - {T_0}^4) - h(T - T_0) \right]$$

$$\dot{m}_v(Y_{i,G} - Y_{i,L}) = [\rho D \nabla Y_i \cdot \mathbf{n}], \tag{6}$$

where $\dot{m}_v$ is the vaporisation rate, I is the laser intensity, h is the heat transfer coefficient, λ is the thermal conductivity and $\mathbf{n}$ is the surface normal vector. The subscripts L and G represent the liquid and gas phase, respectively. The brackets denote the difference $[f] = f_L - f_G$. The recoil pressure works on the vaporising interface and the above constraint is given for the mass fraction. The velocity at the evaporating surface satisfies

$$\dot{m}_v = \rho_L(\mathbf{u}_S - \mathbf{u}_L) \cdot \mathbf{n} = \rho_G(\mathbf{u}_S - \mathbf{u}_G) \cdot \mathbf{n}, \tag{7}$$

where the surface velocity $\mathbf{u}_S$ is the sum of the liquid velocity and the surface regression velocity, i.e. $\mathbf{u}_S = \mathbf{u}_L + \mathbf{s}_L$. The surface regression velocity is given as $\boldsymbol{s}_L = s_L\mathbf{n} = (\dot{m}_v/\rho_L)\mathbf{n}$. Therefore,

$$\mathbf{u}_G - \mathbf{u}_L = -(\rho_G^{-1} - \rho_L^{-1})\dot{m}_v\mathbf{n}. \tag{8}$$

The vapour mass fraction and the vapour pressure at the surface are given by the Clapeyron-Clausius relation.

By solving the set of equations of (1)-(8), the evolution of melt flow kinetics and liquid/gas interface change can be analysed and rationalised. A detailed model description and model parameters can be found in [39].

The CFD model has been applied to the generated powder particle distribution with the cumulative median diameter of 14μm and the maximum powder diameter of 36μm. The grid resolution is 2.5μm. The calculation domain is 440μm × 230μm × 230μm, containing 1.61 million grid points. The laser heat source of 400 W with a scanning speed of 3000 mm/s to simulate the processing condition and study the effect of compositions. The present conditions are in the fast scanning regime, where the interaction of the laser melting and the melt pool dynamics is rather larger to see the difference more clearly. Table 1 lists selected nickel-based superalloys designed for casting, hot working and newly designed for AM. Thermo-physical property of baseline nickel-based superalloy IN718 as well as CMSX-10 and RR1000 has been given in Table 2. Note that all materials parameters are temperature dependent. Laser parameters and processing conditions are shown in Table 3.

Table 1: Selected composition of nickel-based superalloys for AM in the current study in wt-% (Ni Balance)

	Ni	Cr	Co	Al	Ti	Nb	Ta	W	Mo	Hf	Zr	C	B	Re	Fe	Mn	Si	P	S
ABD-850AM [40]	Bal	18.68	17.60	1.29	2.22	0.60	0.44	4.74	1.89	-	-	0.01	0.003	-	-	-	-	-	-
ABD-900AM [40]	Bal	16.96	19.93	2.11	2.39	1.78	1.42	3.08	2.09	-	-	0.05	0.005	-	-	-	-	-	-
CM247LC [40]	Bal	8.30	8.99	5.62	0.75	-	3.16	9.45	0.52	1.32	-	0.07	0.016	-	-	-	-	-	-
CMSX-10 [26]	Bal	2.0	3.0	5.7	0.2	0.1	8.0	8.0	0.4	0.03	-	-	-	6.0	-	-	-	-	-
ExpAM [41]	Bal	9.8	5.0	4.1	-	3.9	7.9	0.9	3.0	-	-	-	-	-	-	-	-	-	-
ExpAM-mod [41]	Bal	9.9	5.2	4.0	-	4.0	7.9	1.2	3.0	-	0.013	0.07	0.015	-	-	-	-	-	-

IN625 [26]	Bal	21.5	1.0	0.4	0.4	3.65	-	-	9.0	-	-	0.1	-	-	5.0	0.5	0.5	0.015	0.015
IN718 [26]	Bal	19.0	1.0	0.5	0.9	5.2	-	-	3.1	-	-	0.08	-	-	16.7	0.35	-	-	-
IN939 [40]	Bal	22.10	18.80	1.76	3.80	0.97	1.37	1.96	-	0.01	0.11	0.16	0.009	-	-	-	-	-	-
MAD542 [42]	Bal	8	8	5	1	2	3	4	5	-	<0.002	0.1	<0.001	-	-	-	<0.005	-	<0.001
RR1000 [26]	Bal	15.0	18.5	3.0	3.6	-	2.0	-	5.0	0.5	0.06	0.027	0.015	-	-	-	-	-	-

Table 2: Thermophysical properties for thermal-fluid flow calculations.

Thermophysical properties	IN718	CMSX-10	RR1000
Solidus temperature, (K)	1533	1633	1506
Liquidus temperature, (K)	1609	1682	1613
Evaporation temperature, (K)	3190	(3190)	(3190)
Density of liquid metal, ($kg.m^{-3}$)	7400	7772	7886
Molar mass, (g/mol)	57.9	63.9	57.1
Specific heat of solid metal, ($J\ kg^{-1}\ K^{-1}$)	625	640	(625)
Specific heat of liquid metal, ($J\ kg^{-1}\ K^{-1}$)	725	700	(725)
Thermal conductivity of solid metal, ($Wm^{-1}\ K^{-1}$)	21.3	21.3	(21.3)
Thermal conductivity of liquid metal, ($Wm^{-1}\ K^{-1}$)	34.5	29.3	32.0
Viscosity, (mPa.s)	7.5	6.0	6.99
Thermal expansion coefficient, (K^{-1})	16.3×10^{-6}	11×10^{-6}	(16.3×10^{-6})
Surface tension, (Nm^{-1})	1.88	1.71	(1.88)
Temperature coefficient of surface tension, ($Nm^{-1}K^{-1}$)	-0.123×10^{-3}	-0.58×10^{-3}	(-0.123×10^{-3})
Enthalpy change of melting, ($J\ kg^{-1}$)	2.1×10^{5}	2.1×10^{5}	(2.1×10^{5})
Enthalpy change of vapourisation, ($J\ kg^{-1}$)	6.4×10^{6}	(6.4×10^{6})	(6.4×10^{6})
Atmospheric pressure, (Nm^{-2})	101300	101300	101300
Ideal gas constant, ($JK^{-1}\ mol^{-1}$)	8.314	8.314	8.314
Boltzmann's constant, ($J\ K^{-1}$)	1.38×10^{-24}	1.38×10^{-24}	1.38×10^{-24}

Note that values in () are extrapolated from IN718 due to the lack of data. Thermophysical property of IN718 is used as a baseline for studying the composition dependency.

Table 3: Parameters used for heat source model in this calculation.

Heat source model parameters	Value
Total beam power, (W)	400
Effective absorption coefficient	0.6
Beam radius, (μm)	35
Beam velocity, (mm s^{-1})	3000

Results

Chemical-process relationship

In order to better understand the chemical-process relationship, the composition dependence of liquid properties – tendency to capture gases in thermal fluid behaviour – including dynamic viscosity and thermal conductivity is systematically studied. According to [27], the dynamic viscosity of liquid, μ, can be approximated empirically as:

$$\log_{10}\mu = \frac{2570}{T[K]} - 0.8224 + 1.75 \times 10^{-3}\, w_{\mathrm{Cr}} + 1.1 \times 10^{-3}\, w_{\mathrm{Fe}} + 10.2 \times 10^{-3}\, w_{\mathrm{W+Re+Nb+Ta+Mo+Hf}} \quad (9)$$

where w_i is the weight percentage of element i. This empirical relation suggests that μ is a function of composition of Cr, Fe and heavy metals (including W, Re, Nb, Ta, Mo and Hf). Figure 2(b) shows the variation of measured density and viscosity in nickel-based superalloys, after [38], and suggests the viscosity is in the range of 5.0 – 8.5 mPa.s. Moreover, CMSX-4 which is denser than IN718 has lower dynamic viscosity, indicating that composition dependence of viscosity is worth further investigating.

Over 100 wrought and cast nickel-based superalloys reported in [26] have been included to study the influence of chemistry on liquid viscosity by applying Equation (9), as ranked in Figure 3(a). It is noted that dynamic viscosity is not directly related to heavy elements following Equation (9), see Figure 3(b). However, it is likely that dynamic viscosity shows some trend when considering Al content, see Figure 3(c), cast superalloys have lower dynamic viscosity than wrought superalloys in general. To the first approximation, one can rank the dynamic viscosity versus maximum nominal γ′ volume fraction, $\phi_{\gamma'}^{max}$ – calculated by:

$$\phi_{\gamma'}^{max} = 4X_{\mathrm{Al+Ti+Ta+Nb}} \quad (10)$$

where $X_{\mathrm{Al+Ti+Ta+Nb}}$ is the atomic percentage of γ′ former elements Al, Ti, Ta and Nb, after [27]. Figure 3(d) indicates that the higher γ′ former elements, the lower dynamic viscosity, indicating that more heavy elements, chromium and iron leads to higher liquid viscosity. With the superalloys successfully processed by AM [5, 16, 26] and highlighted in larger solid dots, it is seen that wrought superalloys with higher viscosity is prone to be more additive manufacturable than cast superalloy with lower dynamic viscosity. Thus far, liquid properties

such as dynamic viscosity may play an important role during AM in terms of process-induced porosity or vapourisation. This can then be used to establish a criterion of additive manufacturability in nickel-based superalloys.

As for the variation in thermal conductivity, following the semi-empirical relation in [27], thermal conductivity (k) at 298K in most nickel-based superalloys is assumed to be a linear function of the Al content. The expression of k is written as

$$k_{298K} = 11.7 - 0.45\, X_{Al} \tag{11}$$

For the liquid alloy, following the calculation in [27], k at liquidus temperature of nickel-based superalloys in this work can be approximated to be a function of X_{Al}, which results in the range of 28 – 35 $W.m^{-1}K^{-1}$.

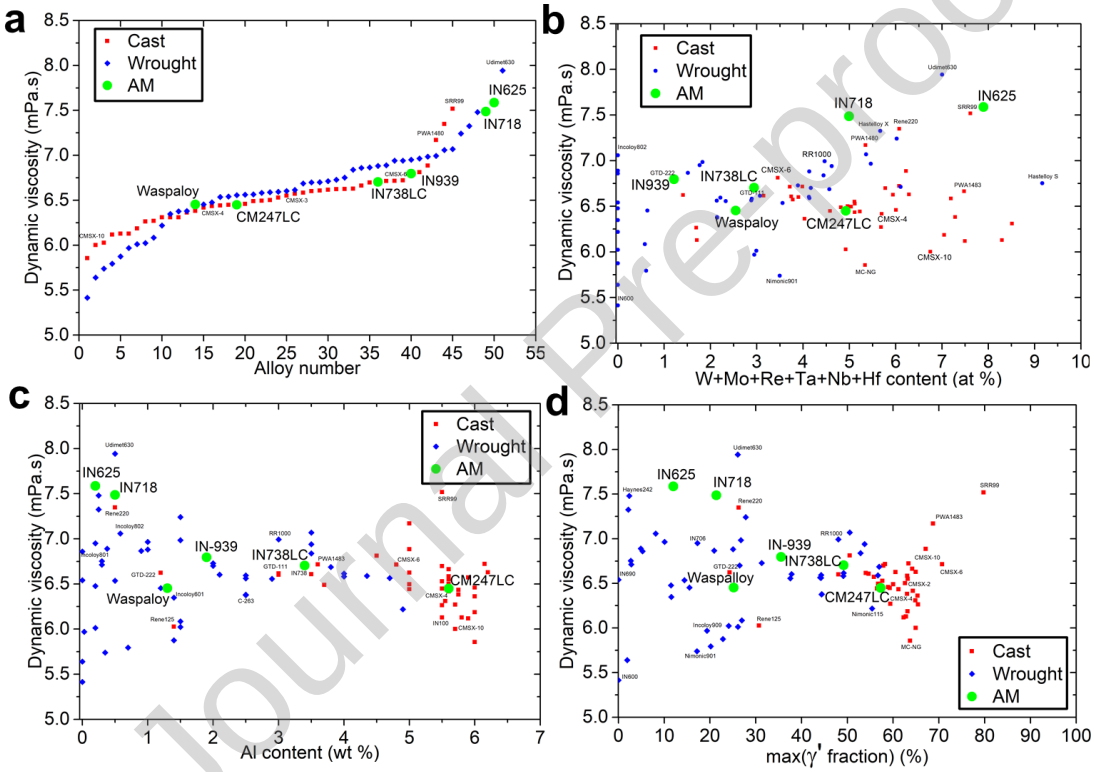

Figure 3: Dynamic viscosity calculated at liquidus temperature for cast, wrought and AM superalloys as a function of (a) alloy number; (b) heavy elements; (c) Al content; (d) γ′ volume fraction.

Effect of thermal-fluid dynamics

It has been reported that some Ni-based superalloys having high viscosity illustrated low level processing-induced 'porosity' [16, 38]. Here, porosity is measured as the volume fraction of void, due to vapourisation and lack of fusion, to the processed volume. With this regard, porosity can be used as a manufacturability criterion for AM [27-29, 39]. To further demonstrate the role of thermo-physical property of nickel-based superalloys, thermal fluid flow model adopted from [39] is used. As mentioned earlier, to link the composition with heat-materials interaction in AM process, we propose to consider fluid flow *via* Reynold number,

Re $= UL/\nu$, and thermal flow via Péclet number, Pe $= UL/\alpha$. In this aspect, U and L refer to velocity and melt pool dimension, varied by the combination of process conditions. Here, $\nu = \mu/\rho$ is the kinematic viscosity, and $\alpha = k/\rho c_p$ is the thermal diffusivity, ρ is density, k is the thermal conductivity, and c_p is the heat capacity. The magnitude of flow velocity, U, and characteristic length scale, L, are used to describe the thermal fluid flow calculated by CFD [39].

To link between chemistry and process, the property of IN718 is used as a baseline and only 'dynamic viscosity' and 'thermal conductivity' are varied while keeping other process parameters constant. Figure 4(a),(b) shows the temperature and velocity fields at t=100μs for varied dynamic viscosity and thermal conductivity. The laser beam is scanned from right to left in the figure. For all the cases, a keyhole is formed in the region of the laser beam (the leftmost part of high temperature region) and a melt pool is formed behind the keyhole (in the right side of the keyhole). The overall melt pool shape is similar among all the cases, but in detail the surface shape and the temperature distribution are slightly different. Similarly, the velocity magnitude shown in Figure 4(b) has some variations among the cases. These variations are quantified next.

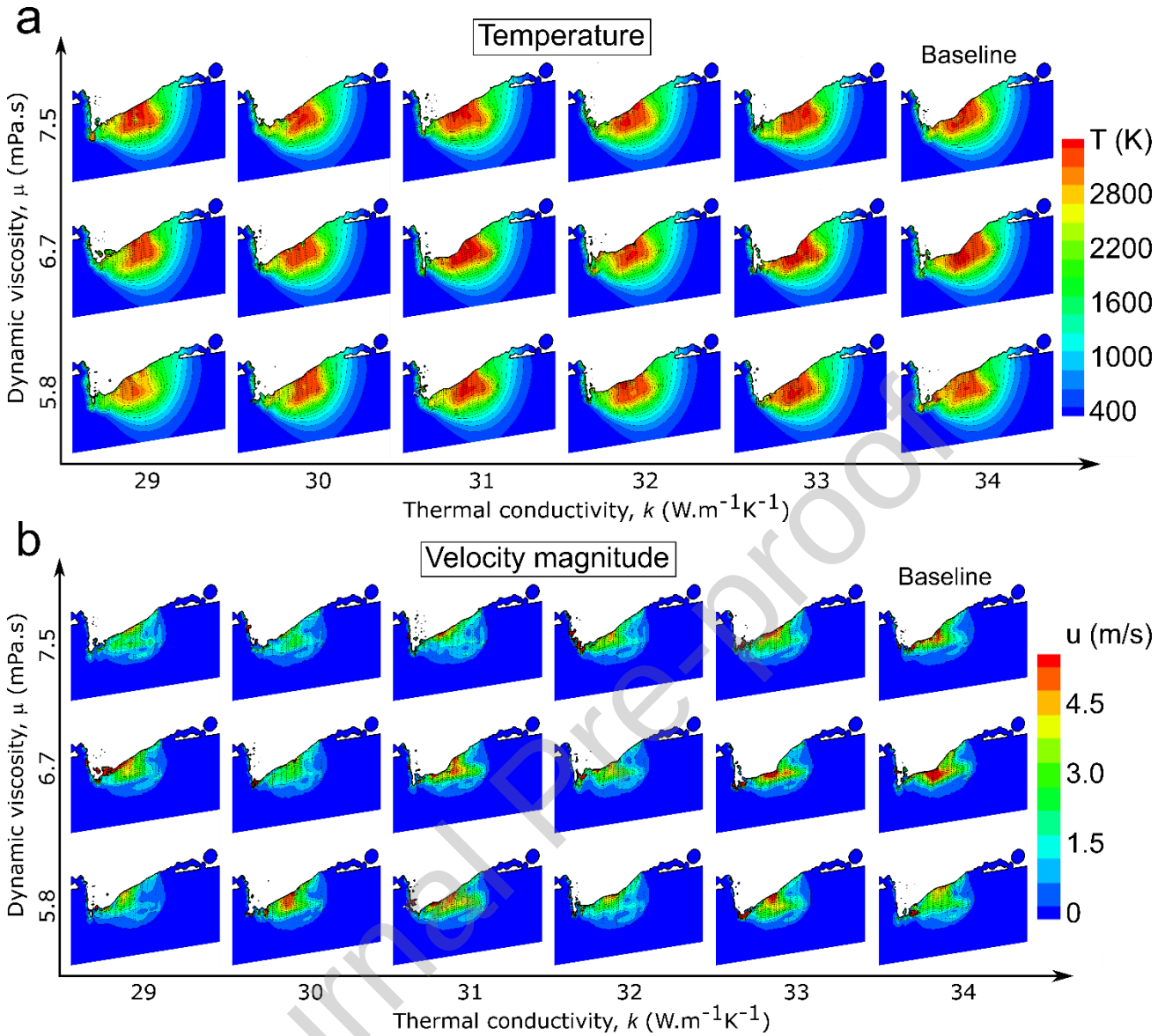

Figure 4: (a) Temperature and (b) velocity magnitude for IN718 with varied dynamic viscosity and thermal conductivity. The visualised plane is at the centre of the laser beam. "Baseline" indicates the case with real IN718 properties.

Figure 5(a)-(d) shows the melt pool volume V_m, the average velocity in the melt pool $\bar{u} = \int \|\mathbf{u}\| dV / V_m$, and the Reynolds and Péclet numbers based on $L = V_m^{\frac{1}{3}}$ and $U = \bar{u}$, respectively. To assess the manufacturability for other Ni-based superalloys as well, two superalloys (CMSX-10 and RR1000) are additionally simulated and included in the following analysis. The circle in the lower left part indicates CMSX-10 and the circle near the centre represents RR1000. The melt pool volume has a tendency to be larger when the dynamic viscosity is larger. And the large melt pool volume region extends from the upper left region (large dynamic viscosity and small thermal conductivity) to the lower right direction (small dynamic viscosity and large thermal conductivity). In contrast, the averaged velocity in the melt pool is larger when the dynamic viscosity is smaller. Still, a similar trend from the upper left to the lower right exists. This indicates

that the flow motion is slower when the dynamic viscosity is larger and the heat transfer is also affected by this. It is clearer if the trends are seen in terms of the process parameters of Reynolds and Péclet numbers. Re has a similar trend as that of the averaged velocity in the melt pool. Pe is also large with a similar tendency from the upper left to the lower right. The Reynolds number has a larger variation in its value than Pe, which indicates that the viscosity and the velocity field are playing a relatively larger role. The reference cases of CMSX-10 and RR1000 exhibit similar trends on the map, which indicates that the above observed trends with respect to viscosity, heat conduction and flow processes are generally applicable to Ni-based superalloys.

Figure 5(e),(f) shows the mass loss rate and the porosity. The mass loss is measured by the vapourisation rate of the metal at the resolved liquid/gas surface. Although a combined effect of the Reynolds and Péclet numbers are present, the mass loss rate and the porosity have a similar tendency with Re and Pe. Larger mass loss and porosity are observed for larger Re and Pe, with relatively larger dependence on Re.

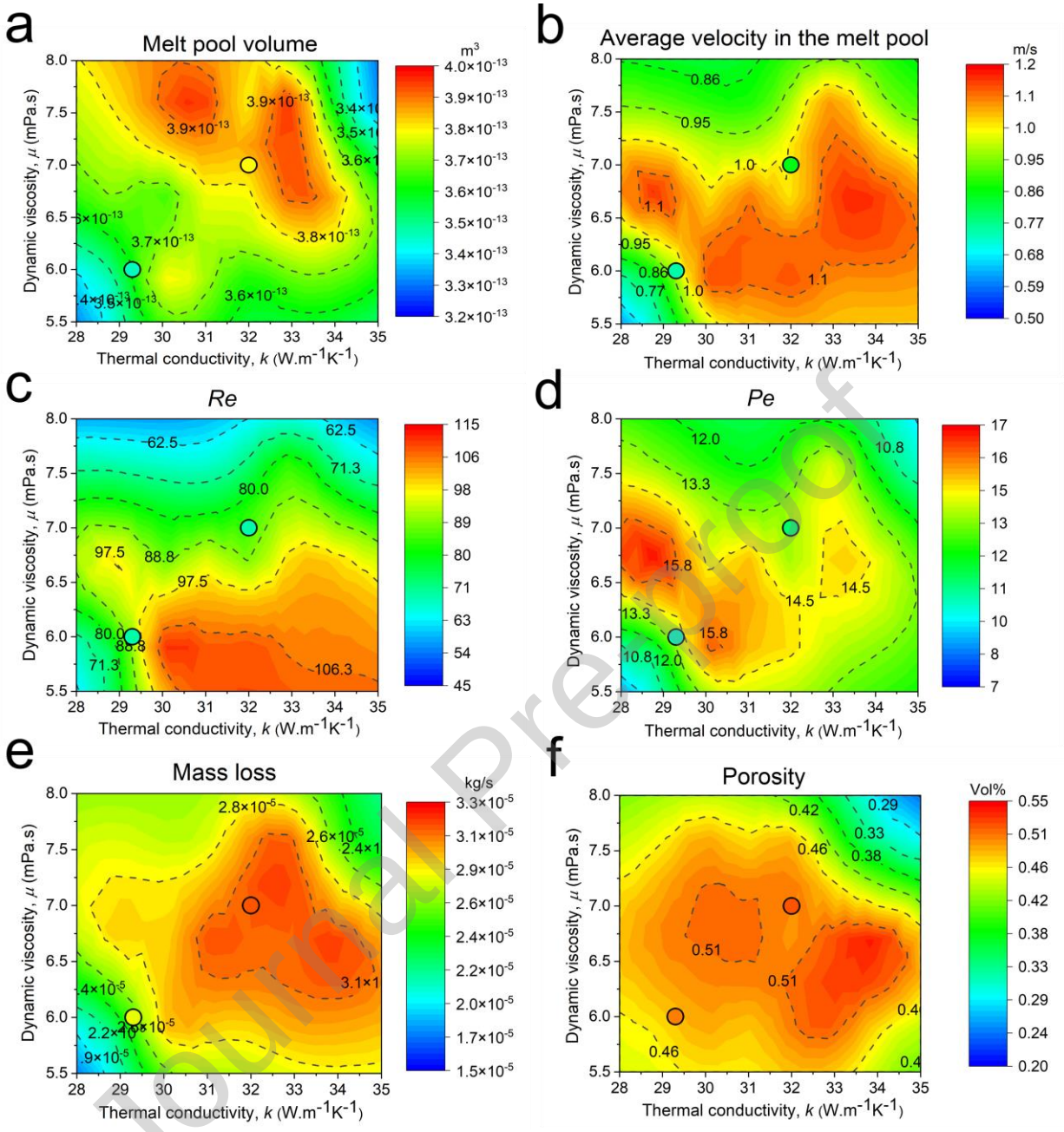

Figure 5: AM process map for superalloys with variations in the dynamic viscosity and thermal conductivity (IN718 property used as a baseline). The circle in the lower left part indicates CMSX-10 and the circle near the centre represents RR1000, for reference. (a) Melt pool volume, (b) average velocity in the melt pool, (c) Reynolds number, (d) Péclet number, (e) mass loss rate and (f) porosity.

Discussion: Additive Manufacturability

Porosity

The proposed AM map in Figure 5 demonstrates a suggested materials-process design diagram for AM based upon thermal fluid dynamics, unlike reported in [38]. Since the additional results of CMSX-10 and RR1000

also confirm that the thermal-fluid dynamic parameters determine the AM process characteristics, various Ni-based superalloys are superposed on the map of porosity with respect to the dynamic viscosity and the thermal conductivity, as shown in Figure 6.

It is suggested that higher dynamic viscosity and thermal conductivity refer to higher additive manufacturability. Here, superalloys with less of both Ti and Al content, which means the less γ′ former elements, give higher dynamic viscosity (> 7.0 mPa.s) and higher thermal conductivity (> 33 $W.m^{-1} K^{-1}$), respectively. For example, highly processible alloys IN625 and IN718 belongs to this regime. When the dissipation in velocity is higher, the fluid flow is stagnated. Therefore, the porosity is lower. Note that due to the lower velocity magnitude, upon cooling from AM, precipitation cracking may be possible. In contrast, the lower dynamic viscosity may lead to acceleration of the fluid flow. Here, if the thermal conductivity is moderate, the porosity is larger. The Reynolds number is larger in this region, which finally leads to larger mass loss. In the region of high viscosity and high thermal conductivity, the porosity and volatile mass loss is relatively lower which corresponds with lower γ′ former elements of wroght alloys. In contrast, when thermal conductivity is lower and viscosity is intermediate, the porosity and volatile mass loss is relatively higher.

Cooling rate in liquid and solid

The cooling rate in the melt pool is evaluated for metallurgical insights. The cooling rate can be a measure to estimate the residual stress [10], where a larger cooling rate results in larger residual stresses [38]. Figure 7(a)(b) shows the cooling rate in the same parameter space as Figure 6. Here, the temporal change of temperature in the periphery of the melt pool is used for the cooling rate calculation, as exemplified in Figure 7(c) using the data for the baseline IN718 case. The cooling rate is negative and the colour bar in the figure is reversed to show the trend in the magnitude. Note that the magnitude is one order smaller in the solid state cooling. The baseline IN718 shows relatively slower cooling compared with other alloys in the middle of the figure. The trend of cooling rate magnitude is correlated to that of Pe (Figure 5(d)) and Re (Figure 5(c)). This is natural since the heat transfer is not only governed by heat conduction, but rather enhanced by the convective effect in the liquid [19,39].

The balance between the fluid flow (Re) and thermal flow (Pe) should be optimum at a given process condition, whilst it should be noted that the relation is non-linear. The suggested similarity among the Ni-based superalloys indicates that this kind of map can be used in understanding the general additive manufacturability by considering the correlation between the alloy compositions and the physical properties.

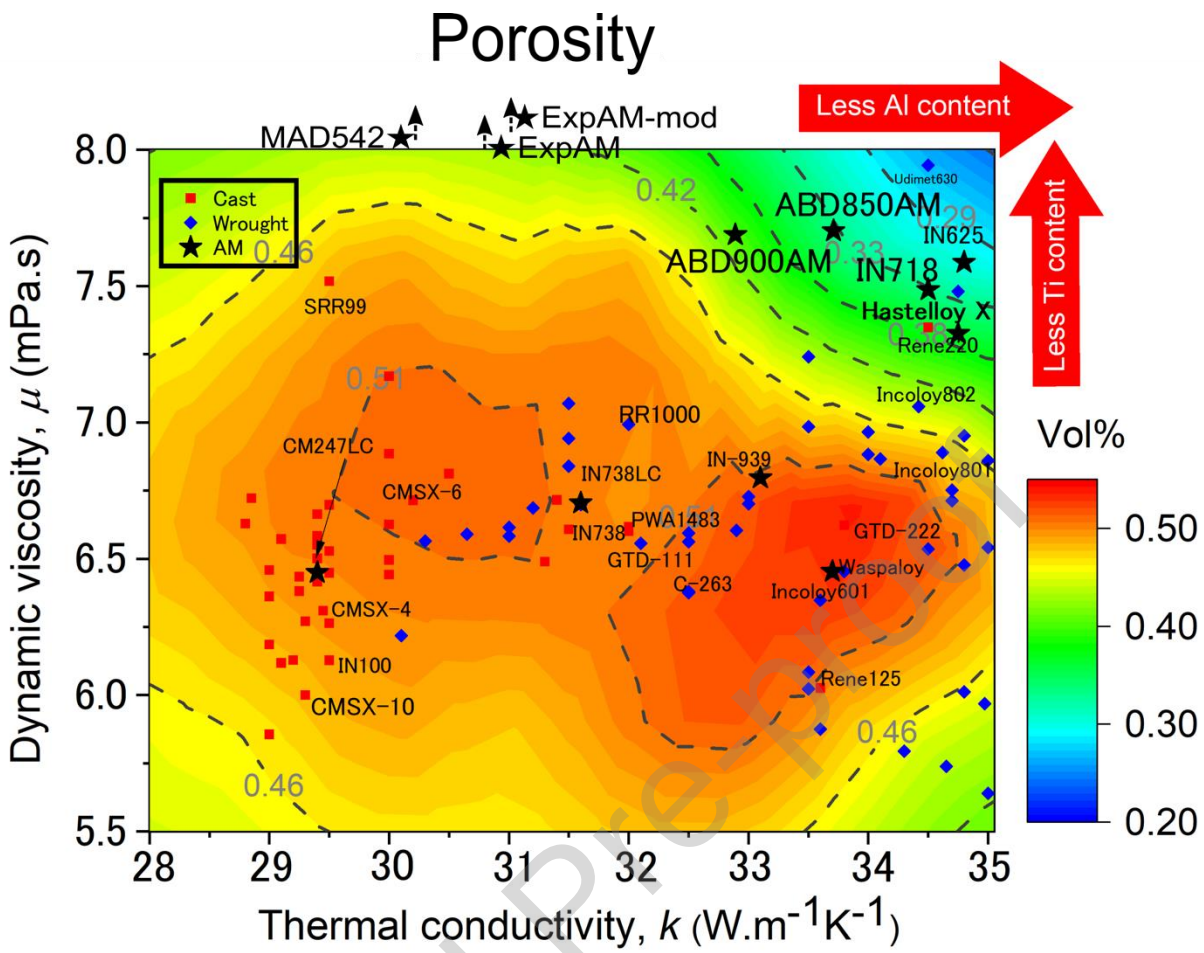

Figure 6: 3D printability diagram for Ni-based superalloys based upon the plot of dynamic viscosity and thermal conductivity, and predicted process-induced porosity from CFD calculation. Other thermophysical properties were kept constant. Note that dynamic viscosities of ExpAM, ExpAM-mod and MAD542 are 8.37, 8.98 and 8.66 mPa.s, respectively.

a

c

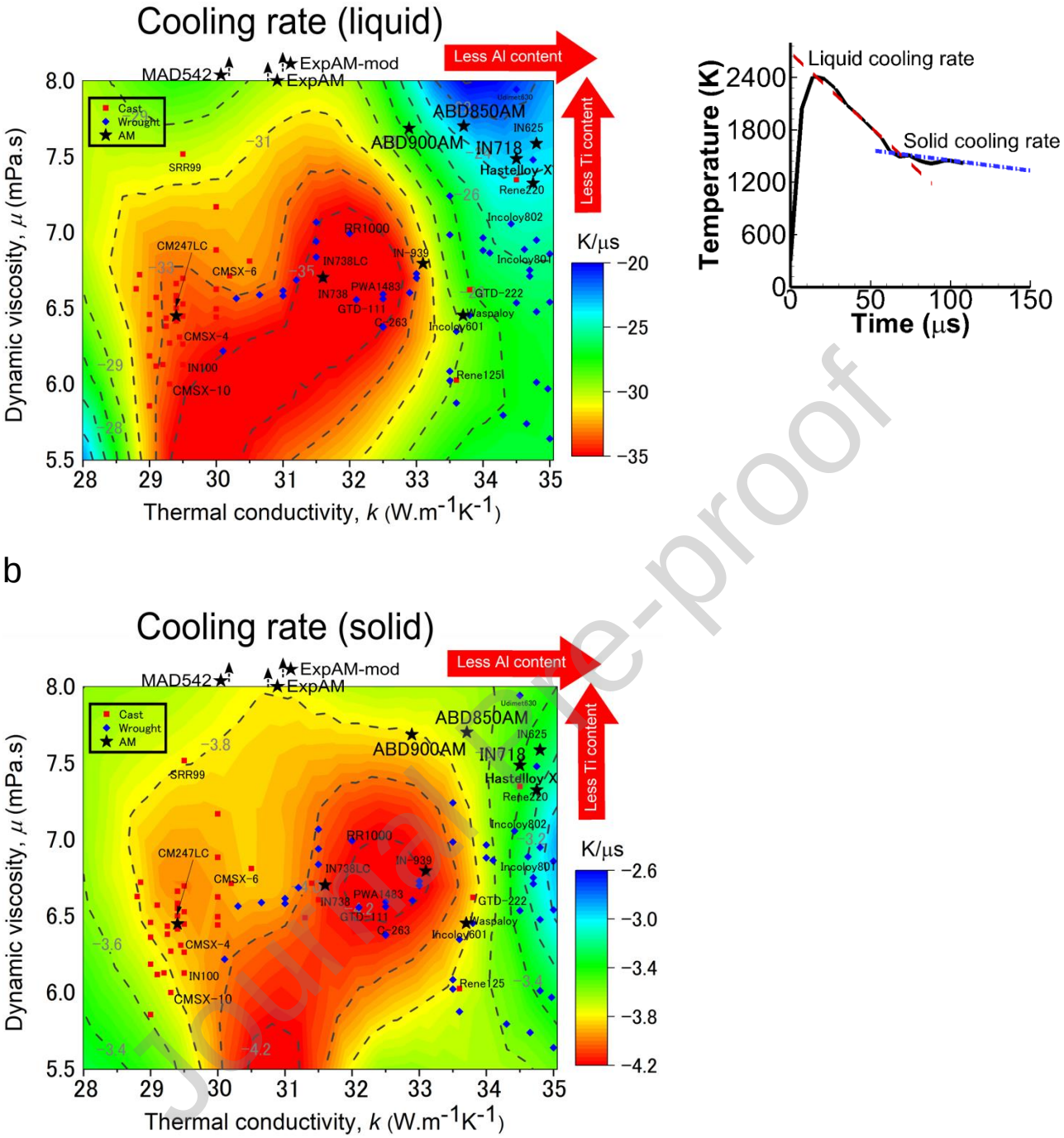

Figure 7: (a) Liquid and (b) solid cooling rates in the periphery of the melt pool plotted for the dynamic viscosity and the thermal conductivity. The temperature profile in (c) is for the baseline IN718 case and the cooling rates are extracted as the temporal gradients. The cooling rate is negative and the colour bar is reversed to show the trend in the magnitude.

Volatile mass loss / vapourisation

The vapour mass loss rate is plotted together with the superalloy names with respect to the thermal conductivity and dynamic viscosity in Figure 8. The mass loss rate (Figure 8) and the porosity (Figure 6) have a strong correlation. IN718, which is most commonly used in AM [16, 43], is both in the region of smaller

mass loss and porosity. The similarity between the porosity and mass loss therefore suggests that the additive manufacturability criterion of porosity can be also applied in terms of estimating mass loss, i.e. less porosity means less mass loss. This is natural since the mass loss is induced by vapourisation and porosity is also caused by vapour. Figure 9 (a)-(d) represents the correlations in terms of Re and Pe for the mass loss, porosity and cooling rates in liquid and solid. As shown in Figure 9(a)(b), the mass loss rate and porosity are larger for the larger Pe and Re conditions, under which the flow motion is relatively large and the heat is moderately stored in a relatively larger melt pool. This shows that the flow motion is dynamically determining the mass loss rate due to vapourisation, which is also reasonable for the porosity formation in flow. The Reynolds and Péclet number dependence for the mass loss rate observed here is similar to that observed for pure elements [39] where the larger Re dominantly determines the larger mass loss, indicating the significance of considering the flow process in AM. For the cooling rates in Figure 9(c)(d), the liquid and solid rates are correlated. The overall trend is similar to mass loss and porosity with some differences in the moderate Re and Pe region. The complication may need further investigation. These relations may quantitatively differ depending on the process conditions. But the physical picture clarified in this study will help to understand the effects of relevant phenomena in AM.

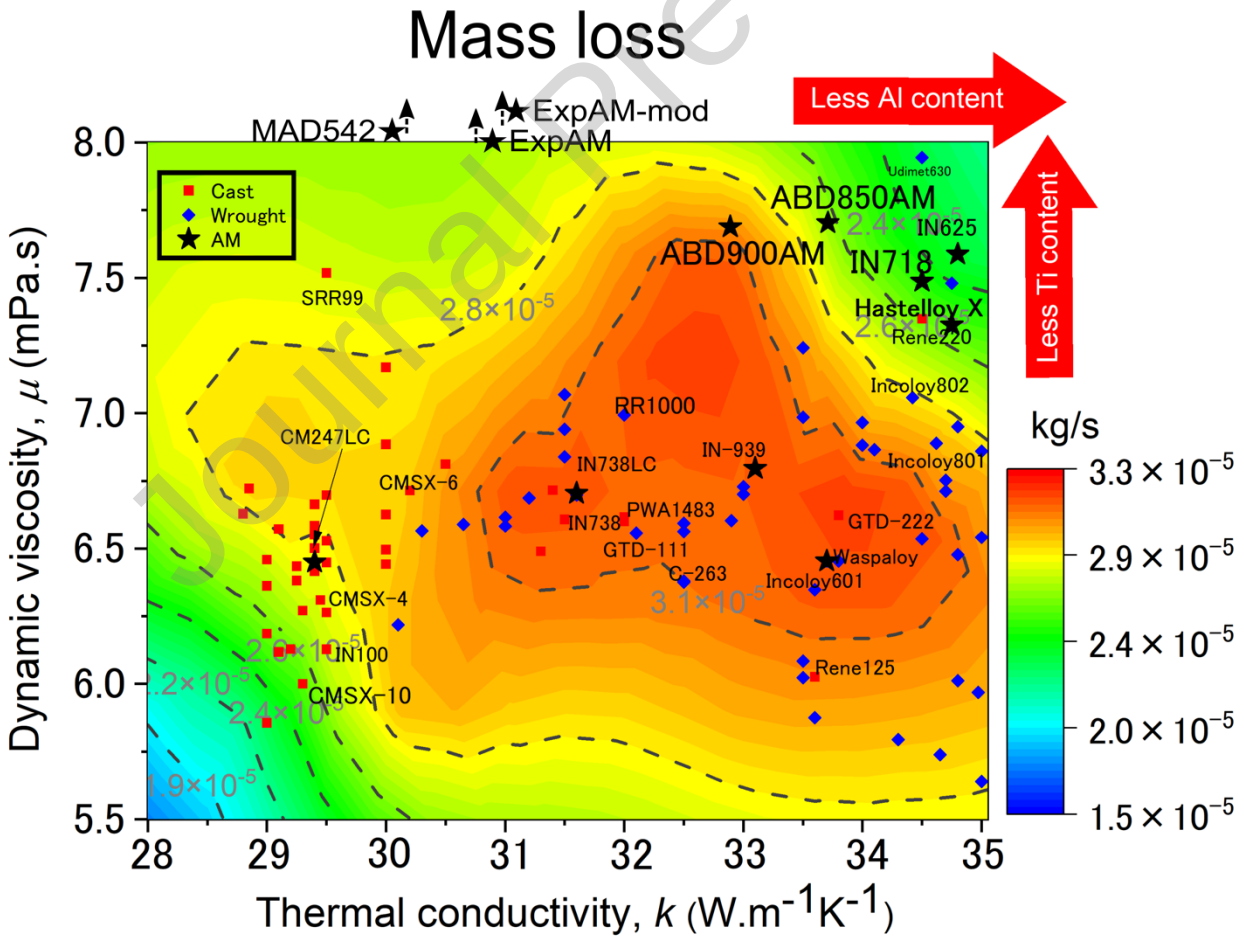

Figure 8: Mass loss rate with respect to thermal conductivity and dynamic viscosity.

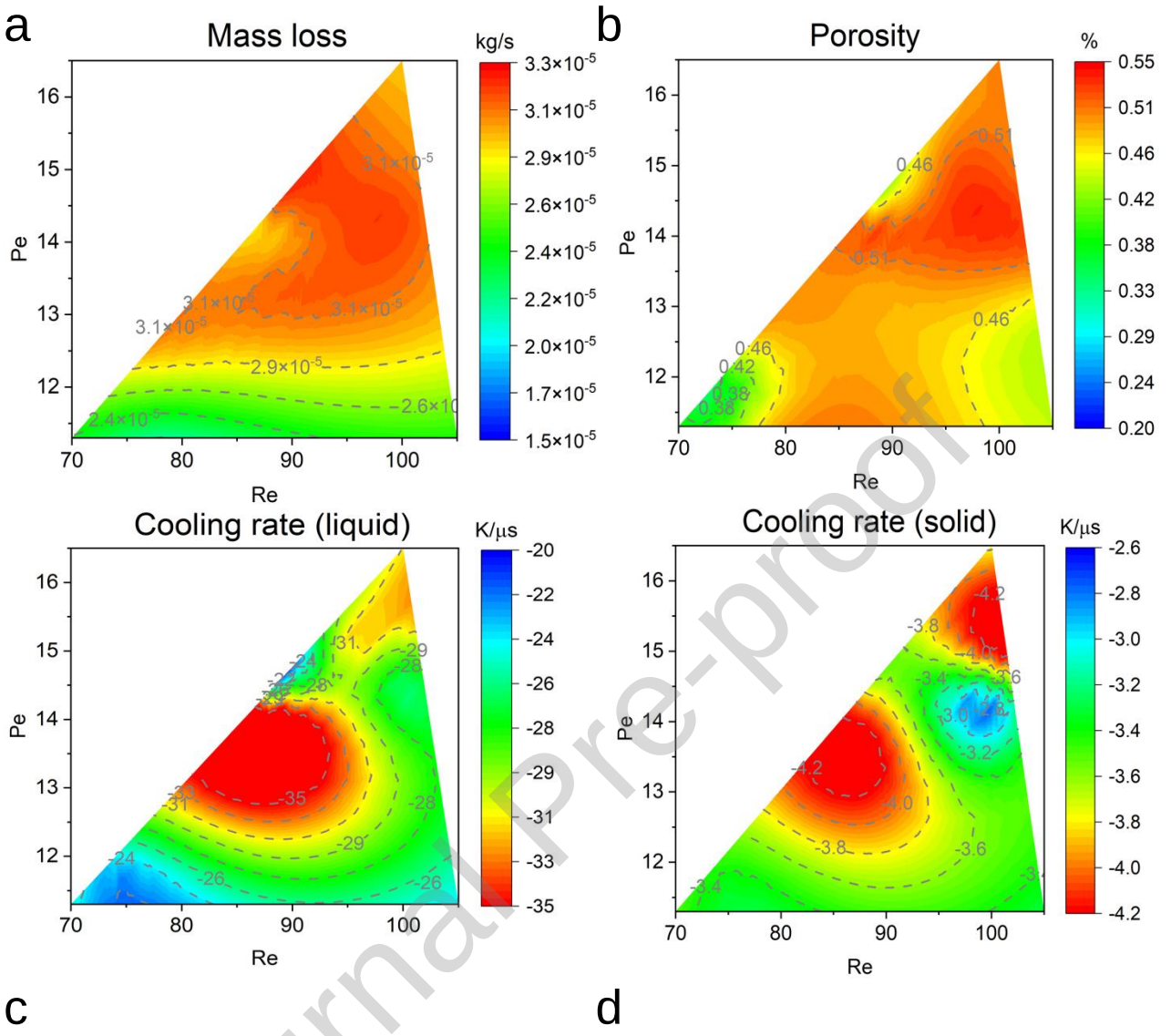

Figure 9: Contour maps of (a) mass loss rate, (b) porosity, (c) cooling rate in liquid and (d) cooling rate in solid with respect to Re and Pe. The cases in this study cover the triangular region in the figure.

Above all, from the CFD calculation and the thermo-physical property estimation, it can be noticed that new nickel-based superalloys designed for AM such as ABD-850AM [40], ABD-900AM [40], ExpAM [41], ExpAM-mod [41] and MAD542 [42] sit in the good additive manufacturability zone based on process-induced porosity (Figure 6), cooling rate (Figure 7) and mass loss results (Figure 8). This emphasises that new alloys are needed for the successful additive manufacturability [17, 40] rationalised by thermal-fluid flow processing maps linked between compostion and process characteristics.

Moreover, apart from the porosity and volatile mass loss criteria which are thermal-fluid flow induced effects, we may consider the manufacturability using the composition effect based upon atomistic understanding [44]. This can lead to another defect related to solid mechanics such as cracking [45,46]. High-throughput

characterisation and mechanical testing are further required to establish the additive manufacturability together with the rationalisation by thermodynamics principle [40].

This composition-process approach, for the first time, can be used to downselect specific materials with specific processing route/condition for a specific use in aerospace, energy or automotive application for novel material design, current process improvement and component repair purposes [47, 48]. These can be used to open a new field of research in metal vapour dynamics in metal additive manufacturing systems, fusion welding as well as investment casting. Hence, the metal additive manufacturability can be tailored using thermophysical properties such as viscosity and thermal conductivity as additive manufacturability indices.

Summary and Conclusion

The thermal-chemical-process relationship of metal of more than 100 nickel-based superalloys has been systematically studied to rationalise the additive manufacturability. The specific conclusions are as follows:

1. The composition dependence of the chemistry-process parameter of liquid dynamic viscosity is systematically investigated to construct chemistry-process maps with respect to alloy number, content of heavy elements, Al content and γ′ volume fraction. The dynamic viscosity is correlated with Al content and thus γ′ volume fraction, with the trend that higher γ′ former elements leads to lower dynamic viscosity. By this, the possible range and trend of dynamic viscosity have been identified for Ni-based superalloys.
2. Chemistry-process parameters using dynamic viscosity versus thermal conductivity or Re and Pe are used to classify the thermal-fluid behaviour. IN718, the most widely used additively manufactured nickel-based superalloy, has been used as a benchmark for CFD calculation. The dynamic viscosity and the thermal conductivity are virtually varied to cover the above identified map range of Ni-based superalloys to see the fluid flow dynamics and their thermal-fluid characteristics were rationalised as a good additive manufacturability. Larger Re and Pe generally leads to larger porosity.
3. Characteristic of mass loss of metal vapour in nickel-based superalloys has been first developed to rationalise the processability using empirical-based model on liquid property such as viscosity, density and thermal conductivity. Larger vapour mass loss is correlated with the higher porosity, which indicates the thermal-fluid flow process, governed by the thermo-physical property, strongly affects the additive manufacturability. Additive manufacturability map based upon porosity and volatile mass loss or vapourisation criteria has been established to link the composition in nickel-based superalloys with their thermo-physical property, which is useful in designing compositions within the range of 0 – 1 wt% of Al and Ti alloying elements of a possible new superalloy for L-PBF AM applications.
4. A higher dynamic viscosity (> 7.0 mPa.s) and thermal conductivity (> 33 $W.m^{-1}K^{-1}$) leads to higher additive manufacturability. This is because it leads to a lower fluid velocity to form porosities and the heat transfer is affected by the velocity. Besides, the liquid to solid transition gives rise to the different

cooling rate and hence residual stress development. The higher viscosity and thermal conductivity, the lower cooling rates both in liquid and solid state. With that, the thermal-fluid modelling can also be used to assess a suitable processing window for a specific alloy.

5. It is suggested that new nickel-based superalloys is needed for the successful additive manufacturability as the legacy alloys were optimised for traditional processes such as casting, forming or forging. The chemistry-process dimensionless parameters – Re and Pe – can be used as design indices for new AM superalloys.

CRediT authorship contribution statement

Chinnapat Panwisawas: Conceptualization, Methodology, Investigation, Writing- Original draft preparation, Funding acquisition. **Yilun Gong:** Resources, Writing- Reviewing and Editing. **Yuanbo Tony Tang:** Visualization, Writing- Reviewing and Editing. **Roger C. Reed:** Conceptualization, Writing- Reviewing and Editing, Funding acquisition. **Junji Shinjo**: Formal analysis, Software, Validation, Visualisation, Writing- Reviewing and Editing

Declaration of Competing Interest

☒The authors declare that they have no known competing financial interests or personal relationships that could have appeared to influence the work reported in this paper.

☐The authors declare the following financial interests/personal relationships which may be considered as potential competing interests:

Acknowledgments

Chinnapat Panwisawas and Yuanbo Tony Tang would like to acknowledge the grant from Innovation Fellowship funded by Engineering and Physical Science Research Council (EPSRC), UK Research and Innovation (grant number: EP/S000828/2). Yilun Gong, Roger Reed and Junji Shinjo would like to acknowledge the grant from the Next Generation Tatara Co-Creation Centre (NEXTA), which is established with Grant-in-aid for the Promotion of Regional Industries and University from Cabinet Office, Japan.

Competing interests

The authors declare no conflict of interest.

Data Availability

The datasets generated during and/or analysed during the current study are available from the corresponding author on reasonable request.

References

[1] J.B. Roca, P. Vaishnav, E.R.H. Fuchs, M.G. Morgan, Policy needed for additive manufacturing, Nat. Mater. 15 (2016) 815-818. https://doi.org/10.1038/nmat4658

[2] A. Agrawal, A. Choudhary, Perspective: Materials informatics and big data: Realization of the "fourth paradigm" of science in materials science, APL Materials 4 (2016) 053208. https://doi.org/10.1063/1.4946894

[3] T.M. Pollock, Alloy design for aircraft engines, Nat. Mater. 15 (2016) 809-815. https://doi.org/10.1038/nmat4709

[4] S.S. Babu, Scripta Viewpoint Set: Materials science aspects related to additive manufacturing, Scr. Mater. 135 (2017) 97–99. https://doi.org/10.1016/j.scriptamat.2017.01.007

[5] S. Tammas-Williams, I. Todd, Design for additive manufacturing with site-specific properties in metals and alloys, Scr. Mater. 135 (2017) 105–110. https://doi.org/10.1016/j.scriptamat.2016.10.030

[6] M.M. Kirka, P. Nandwana, Y. Lee, R.R. Dehoff, Solidification and solid-state transformation sciences in metals additive manufacturing, Scr. Mater. 135 (2017) 130–134. https://doi.org/10.1016/j.scriptamat.2017.01.005

[7] Z. Hu, S. Mahadevan, Uncertainty quantification in prediction of material properties during additive manufacturing, Scr. Mater. 135 (2017) 135–140. https://doi.org/10.1016/j.scriptamat.2016.10.014

[8] B.H. Jared, *et al*. Additive manufacturing: Toward holistic design Scr. Mater. 135 (2017) 141–147. https://doi.org/10.1016/j.scriptamat.2017.02.029

[9] C. Panwisawas, C.L. Qiu, Y. Sovani, J.W. Brooks, M.M. Attallah, H.C. Basoalto, On the role of thermal fluid dynamics into the evolution of porosity during selective laser melting, Scr. Mater. 105 (2015) 14-17. http://dx.doi.org/10.1016/j.scriptamat.2015.04.016

[10] C. Qiu, C. Panwisawas, M. Ward, H.C. Basoalto, J. W. Brooks, M.M. Attallah, On the role of melt flow into the surface structure and porosity development during selective laser melting, Acta Mater. 96 (2015) 72-79. http://dx.doi.org/10.1016/j.actamat.2015.06.004

[11] C. Ma, L. Chen, C. Cao, X. Li. Nanoparticle-induced unusual melting and solidification behaviours of metals. Nat. Commun. 8 (2017) 14178. https://doi.org/10.1038/ncomms14178

[12] S.A. Khairallah, A.T. Anderson, A.Rubenchik, W.E. KingK, Laser powder-bed fusion additive manufacturing: Physics of complex melt flow and formation mechanisms of pores, spatter, and denudation zones, Acta Mater. 108 (2016) 36-45. http://dx.doi.org/10.1016/j.actamat.2016.02.014

[13] M.J. Matthews, G. Guss, S.A. Khairallah, A.M. Rubenchik, P.J. Depond, W.E. King, Denudation of metal powder layers in laser powder bed fusion processes, Acta Mater. 114 (2016) 33-42. http://dx.doi.org/10.1016/j.actamat.2016.05.017

[14] T.T. Roehling, S.S.Q. Wu, S.A. Khairallah, J.D. Roehling, S.S. Soezeri, M.F. Crumb, M.J. Matthews, Modulating laser intensity profile ellipticity for microstructural control during metal additive manufacturing, Acta Mater. 128 (2017) 197-206. https://doi.org/10.1016/j.actamat.2017.02.025

[15] I. Choquet, A.J. Shirvan, H. Nilsson, On the choice of electromagnetic model for short high-intensity arcs, applied to welding, J. Phys. D: Appl. Phys 45 (2012) 205203. http://dx.doi.org/10.1088/0022-3727/45/20/205203

[16] S. Sanchez, P. Smith, Z. Xu, G. Gaspard, C. J. Hyde, W.W. Wits, I.A. Ashcroft, H. Chen, A.T. Clare, Powder Bed Fusion of nickel-based superalloys: A review, International Journal of Machine Tools and Manufacture, (2021) 103729. https://doi.org/10.1016/j.ijmachtools.2021.103729

[17] C. Panwisawas, Y.T. Tang, R.C. Reed, Metal 3D printing as a disruptive technology for superalloys, Nat. Commun. 11 (2020) 2327. https://doi.org/10.1038/s41467-020-16188-7

[18] H. Wei, J. Mazumder, T. DebRoy, Evolution of solidification texture during additive manufacturing. Sci. Rep. 5 (2015) 16446. https://doi.org/10.1038/srep16446

[19] T. Mukherjee, J. Zuback, A. De, T. DebRoy, Printability of alloys for additive manufacturing. Sci. Rep. 6 (2016) 19717. https://doi.org/10.1038/srep19717

[20] P.A. Hooper, Melt pool temperature and cooling rates in laser powder bed fusion, Addit. Manuf. 22 (2018) 548-559. https://doi.org/10.1016/j.addma.2018.05.032

[21] I. Todd, Metallurgy: No more tears for metal 3D printing, Nature 549 (2017) 342-343. https://doi.org/10.1038/549342a

[22] I. Todd, Printing steels. Nature Mater. **17** (2018) 13–14. https://doi.org/10.1038/nmat5042

[23] S. Yip, Synergistic science, Nat. Mater. 2 (2003) 3-5. https://doi.org/10.1038/nmat778

[24] S. Yip, M.P. Short, Multiscale materials modelling at the mesoscale, Nat. Mater. 12 (2013) 774-777. https://doi.org/10.1038/nmat3746

[25] C. Panwisawas, C. Qiu, M.J. Anderson, Y. Sovani, R.P. Turner, M.M. Attallah, J.W. Brooks, H.C. Basoalto, Mesoscale modelling of selective laser melting: Thermal fluid dynamics and microstructural evolution, Comput. Mater. Sci. 126 (2017) 479-490. http://dx.doi.org/10.1016/j.commatsci.2016.10.011

[26] R.C. Reed, The Superalloys: Fundamentals and Applications, Cambridge University Press 2008.

[27] K.C. Mills, Y.M. Youssef, Z. Li, Y. Su, Calculation of Thermophysical Properties of Ni-based Superalloys, ISIJ International 46 (2006) 623–632. https://doi.org/10.2355/isijinternational.46.623

[28] J. Sato, T. Omori, K. Oikawa, I. Ohnuma, R. Kainuma, K. Ishida, Cobalt-base high-temperature alloys Science 312 (2006) 90-91. https://doi.org/10.1126/science.1121738

[29] J.J. Valencia, P.N. Quested, Thermophysical Properties, ASM Handbook, Volume **15**: Casting, 468-481 (2008). https://doi.org/10.31399/**asm**.hb.**v15**.a0005240

[30] Q. Guo, C. Zhao, M. Qu, L. Xiong, S.M.H. Hojjatzadeh, L.I. Escano, N.D. Parab, K. Fezzaa, T. Sun, L. Chen, In-situ full-field mapping of melt flow dynamics in laser metal additive manufacturing, Addit. Manuf. 31 (2020) 100939. https://doi.org/10.1016/j.addma.2019.100939

[31] P.S. Cook, A.B. Murphy, Simulation of melt pool behaviour during additive manufacturing: Underlying physics and progress, Addit. Manuf. 31 (2020) 100909. https://doi.org/10.1016/j.addma.2019.100909

[32] Y. Zhao, K. Aoyagi, K. Yamanaka, A. Chiba, A Role of operating and environmental conditions in determining molten pool dynamics during electron beam melting and selective laser melting, Addit. Manuf. 36 (2020) 101559. https://doi.org/10.1016/j.addma.2020.101559

[33] S.A. Khairallah, A.A. Martin, J.R.I. Lee, G. Guss, N.P. Calta, J.A. Hammons, M.H. Nielsen, K. Chaput, E. Schwalbach, M.N. Shah, M.G. Chapman, T.M. Willey, A.M. Rubenchik, A.T. Anderson, Y.M. Wang, M.J. Matthews, W.E. King, Controlling interdependent meso-nanosecond dynamics and defect generation in metal 3D printing, Science 368 (2020) 660-665. https://doi.org/10.1126/science.aay7830

[34] C. Panwisawas, Y.T. Tang, J. Ghoussoub, R.C. Reed, Additive manufacturability of Nickel-based superalloys: Composition-process induced vapourization, S. Tin (Ed.), Superalloys 2020. The Minerals, Metals & Materials Series, Springer, Champian (2020), https://doi.org/10.1007/978-3-030-51834-9_100

[35] F. Verhaeghe, T. Craeghs, J. Heulens, L. Pendelaers, A pragmatic model for selective laser melting with evaporation, Acta Mater. 57 (2009) 6006-6012. https://doi.org/10.1016/j.actamat.2009.08.027

[36] Z. Gan, O.L. Kafka, N. Parab *et al.* Universal scaling laws of keyhole stability and porosity in 3D printing of metals. *Nat Commun* 12 (2021) 2379. https://doi.org/10.1038/s41467-021-22704-0

[37] A.T. Polonsky, T.M. Pollock, Closing the science gap in 3D metal printing, Science 368 (2020) 583-584. https://doi.org/10.1126/science.abb4938

[38] H.C. Basoalto, C. Panwisawas, Y. Sovani, M.J. Anderson, R.P. Turner, B. Saunders, J.W. Brooks, A computational study on the three-dimensional printability of precipitate strengthened nickel-based superalloys, Proc. R. Soc. A 474-2220 (2018) 20180295. http://dx.doi.org/10.1098/rspa.2018.0295

[39] J. Shinjo, C. Panwisawas, Digital materials design by thermal-fluid science for multi-metal additive manufacturing, Acta Mater., 210 (2021) 116825. https://doi.org/10.1016/j.actamat.2021.116825

[40] Y.T. Tang, C. Panwisawas, J. Ghoussoub, Y. Gong, J. Clark, A. Németh, D.G. McCartney, R.C. Reed, Alloys-By-Design: Application to New Superalloys for Additive Manufacturing. Acta Mater. 203 (2020) 116468. https://doi.org/10.1016/j.actamat.2020.09.023

[41] N. Zhou, A.D. Dicus, S.A.J. Forsik, T. Wang, G.A. Colombo, M.E. Epler, Development of a New Alumina-Forming Crack-Resistant High-γ' Fraction Ni-Base Superalloy for Additive Manufacturing, S. Tin (Ed.), Superalloys 2020. The Minerals, Metals & Materials Series, Springer, Champian (2020), https://doi.org/10.1007/978-3-030-51834-9_102

[42] J. Xu, H. Gruber, R. Lin Peng, J. Moverare, A Novel γ'-Strengthened Nickel-Based Superalloy for Laser Powder Bed Fusion. Materials. 13(21) (2020) 4930. https://doi.org/10.3390/ma13214930

[43] G.J. Brunck, A. Kamel, Deposition of Superalloys using Powdered Flux and Metal, US Patent, US2013/0140278 A1, (2013).

[44]A. Janotti, M. Krčmar, C. L. Fu, R. C. Reed, Solute Diffusion in Metals: Larger Atoms Can Move Faster, Phys. Rev. Lett. 92 (2004) 085901. https://doi.org/10.1103/PhysRevLett.92.085901

[45] S.-L. Liu, C.-Y. Wang, T. Yu, Influence of the alloying elements Re, Co and W on the propagation of the Ni/Ni_3Al interface crack, RSC Advances 5 (2015) 52473. https://doi.org/10.1039/C5RA07323E

[46] P.J. Withers, Fracture mechanics by three-dimensional crack-tip synchrotron X-ray microscopy, Phil. Trans. R. Soc. A 373 (2015) 20130157. https://doi.org/10.1098/rsta.2013.0157

[47] S.A.M. Tofail, E.P. Koumoulos, A. Bandyopadhyay, S. Bose, L. O'Donoghue, C.Charitidis, Additive manufacturing: scientific and technological challenges, market uptake and opportunities, Materials Today 21(1) (2018) 22-37. https://doi.org/10.1016/j.mattod.2017.07.001

[48] M. Attaran, The rise of 3-D printing: The advantages of additive manufacturing over traditional manufacturing, Business Horizons 60(5) (2017) 677-688. https://doi.org/10.1016/j.bushor.2017.05.011